



SCIPP 95/14
 April 1995
 hep-ph/9504434

Top Quark Production and Decay at Next-to-leading Order in e^+e^- Annihilation

Carl R. Schmidt ¹

Santa Cruz Institute for Particle Physics
 University of California, Santa Cruz, CA 95064, USA

Abstract

We study the effects of QCD corrections to the process $e^+e^- \rightarrow t\bar{t} + X \rightarrow b\bar{\ell}^+\nu\bar{b}\ell^-\bar{\nu} + X$ above threshold. We show how to treat consistently to $\mathcal{O}(\alpha_s)$ the gluon radiation in both the production and the decay of the top quarks, while maintaining all angular correlations in the event. At this order there is an ambiguity in the event reconstruction whenever a real gluon occurs in the final state. We study the effects of this ambiguity on the top mass and helicity angle distributions. For a top mass of 175 GeV and collider energy of 400 GeV the gluon radiation is emitted predominantly in the decay of the top quarks.

¹Supported in part by the U.S. Department of Energy.

1 Introduction

Recently, the CDF[1] and the D0[2] collaborations at Fermilab announced the observation of the top quark in $p\bar{p}$ collisions at the Tevatron. Both groups saw a statistically significant excess of dilepton and lepton+jets events with the proper kinematic properties and bottom quark tags needed to indicate $t\bar{t}$ production. Furthermore, they were able to extract mass values for the top quark by fitting to events consisting of a single lepton plus four jets. The D0 group found a mass of $199^{+19}_{-21} \pm 22$ GeV, while CDF obtained a mass of $176 \pm 8 \pm 10$ GeV. Both of these mass measurements are in excellent agreement with the value of $175 \pm 11^{+17}_{-19}$ GeV obtained indirectly from a global fit[3] to the electroweak data from LEP and SLAC. The direct observation of the top quark at the Tevatron heralds the start of a new era in the study of flavor physics.

The top quark is certainly unique among the six known quarks. It is by far the heaviest; more than 30 times as massive as the bottom quark and even more massive than the W and Z bosons. Correspondingly, the top quark also has the largest coupling to the symmetry breaking sector of all the known particles. This large coupling to the Higgs sector may give rise to deviations from its expected behavior, thereby offering clues to symmetry breaking, fermion mass generation, quark family replication, and other deficiencies of the Standard Model. For example, in top-color and extended technicolor (ETC) models the top quark may have non-standard couplings to the weak vector bosons[4] or there may be resonant enhancement of $t\bar{t}$ production[5]. It is of utmost importance to examine the top quark properties

as precisely as possible.

A more basic consequence of the large top quark mass is its short lifetime. For large mass the lifetime of the top quark scales as $[1.7 \text{ GeV} \cdot (m_t/175 \text{ GeV})^3]^{-1}$, and so the top quark decays very rapidly to a bottom quark and a W . Thus, unlike the lighter quarks which form hadronic bound states before decaying, the top quark behaves more like a heavy lepton, decaying as an unbound fermion. In fact, it decays long before depolarization, so that its spin information can be easily reconstructed from the momenta of its decay products. This fact will be extremely useful for extracting information about the top quark parameters.

An ideal place to study the top quark is in e^+e^- collisions[6, 7], where the colorless initial state provides a clean event environment, and there is the possibility of initial-state polarization. By varying the beam energy it is possible to scan the threshold region or to study the top above threshold. There have been many studies of top production near threshold, where the resonance behavior can be calculated in perturbative QCD and the top mass can be obtained to high accuracy[8]. In this paper we will instead concentrate on the continuum $t\bar{t}$ production. At tree level the event is characterized by six final-state particles arising from the process $e^+e^- \rightarrow t\bar{t} \rightarrow bW^+\bar{b}W^- \rightarrow b\ell^+\nu\bar{b}\ell^-\bar{\nu}$. These six particles contain a wealth of information in their relative momenta, angles, and polarizations. By reconstructing the helicity angles of the top quarks and the W 's, it is straightforward to extract the top quark parameters.

Although the top quark is produced and decays essentially as an unbound

fermion, it still feels the strong interactions and will radiate gluons—both in its production phase and its decay phase. Thus, it is useful to see how the tree-level picture and experimental analysis will be affected by QCD corrections. The $\mathcal{O}(\alpha_s)$ corrections to the production have been studied in several papers, including analyses of the effects on production angle distributions[9] and polarizations[10]. Similarly, studies of the $\mathcal{O}(\alpha_s)$ corrections on the top decay have been done, with analyses of energy distributions, and angular distributions from polarized tops[11]. However, the top production and decays do not occur in isolation from each other. For events with an extra gluon jet it is not *a priori* obvious whether to assign the extra jet to the production, the t decay, or the \bar{t} decay. At the very least, the extra jets will add one more degree of complexity to the event reconstruction process. Therefore, it is necessary to assess the impact of these radiative corrections on the full event[12].

To this end we have constructed a next-to-leading order (NLO) Monte Carlo which treats consistently to $\mathcal{O}(\alpha_s)$ the radiative corrections to both production and decay of the top quarks. To set the stage for this NLO analysis we begin by reviewing the salient features of the $e^+e^- \rightarrow t\bar{t}$ event at tree level using helicity decomposition in section 2. Then in section 3 we analyze the cross section at next-to-leading order and give the details of the Monte Carlo, describing the approximations used and the methods for subtracting the infrared (IR) divergences in production and decay. We also include two appendices with the helicity amplitudes for top production and decay with real gluons. In section 4 we use the Monte Carlo to study the effects of gluon radiation on the top quark mass measurement and to

re-examine the helicity angle distributions at next-to-leading order. In this section we assume that the only ambiguities are in the placement of the extra gluon jet, that the W 's and bottom quarks are correctly identified, and we investigate how the distributions vary with the algorithm used for assigning the gluon jet. Then in section 5 we make another pass through the mass distributions with more realistic experimental assumptions for the event. The purpose of this section is to identify which physical inputs have the largest effect on the continuum measurement of the top mass. In section 6 we offer our conclusions.

2 Review of the tree-level analysis

Even at tree level the full $e^+e^- \rightarrow t\bar{t}$ event is quite complex. The six-particle final state can be characterized in many possible ways by the relative momenta and angles in the event. It is an important conceptual problem to clarify which pieces of information are most important, and how all of the various kinematic measurements available cooperate to illuminate the basic physics. The solution to this problem is suggested by the fact that the event is actually a series of on-shell two-body decays: $\gamma^*, Z^* \rightarrow t\bar{t}$, $t \rightarrow bW^+$, and $W^+ \rightarrow \ell^+\nu$. Thus, by considering intermediate states of definite helicities, the event is highly constrained simply by conservation of angular momentum. The different helicity states are revealed by the angular distributions of their decay products, while the relative amplitudes for the different helicity combinations are easily related to the couplings at the top quark production and decay vertices. In this section we describe this tree-level

helicity analysis. Although this has been discussed before in the literature, most notably by Kane, Ladinsky, and Yuan[13], we will review it here for pedagogical purposes and to set the notation for the discussion of QCD corrections.

The dominant effects of new physics on the process $e^+e^- \rightarrow t\bar{t} \rightarrow bW^+\bar{b}W^-$ can be described in terms of form factors included at the production and decay vertices. The $t \rightarrow bW^+$ decay vertex can be written

$$i\mathcal{M}^{W\mu} = i\frac{g}{\sqrt{2}}\left\{\gamma^\mu[F_{1L}^W P_L + F_{1R}^W P_R] + \frac{i\sigma^{\mu\nu}q_\nu}{2m_t}[F_{2L}^W P_R + F_{2R}^W P_L]\right\}, \quad (1)$$

where $P_{R,L} = (1 \pm \gamma_5)/2$, and we have neglected a third pair of form factors which do not contribute to decays to on-shell W 's or massless fermions. We have chosen the subscripts L, R of the form factors so that they indicate the helicity of the outgoing bottom quark in the limit $m_b = 0$, which we will use in all of our matrix element calculations. At tree level in the standard model $F_{1L}^W = 1$ and all other form factors are zero. In fact, $F_{1R}^W = F_{2R}^W = 0$ to all orders in the standard model in the limit of massless bottom quark. The antitop form factors are identical to these in the limit of CP invariance.

Similarly, the $\gamma, Z \rightarrow t\bar{t}$ production vertices can be written

$$i\mathcal{M}^{i\mu} = ie\left\{\gamma^\mu[F_{1V}^i + F_{1A}^i\gamma_5] + \frac{i\sigma^{\mu\nu}q_\nu}{2m_t}[F_{2V}^i + F_{2A}^i\gamma_5]\right\}, \quad (2)$$

where each form factor can be a function of the center-of-mass energy \sqrt{s} , the superscript is $i = \gamma, Z$, and we have again dropped a third pair of form factors which are unobservable. At tree level in the standard model $F_{1V}^\gamma = \frac{2}{3}$, $F_{1V}^Z = (\frac{1}{4} - \frac{2}{3}s_w^2)/s_w c_w$, and $F_{1A}^Z = (-\frac{1}{4})/s_w c_w$, and all others are zero. Here, $s_w = \sin \theta_w$

and $c_w = \cos \theta_w$. In the limit of CP invariance $F_{2A}^i = 0$. The production analysis is simplified if we consider separately the two possible helicities of the incoming electrons, so that the contribution of the photon and the Z add coherently. We define new form factors by

$$\begin{aligned}\mathcal{F}_{ij}^L &= -F_{ij}^\gamma + \left(\frac{-\frac{1}{2} + s_w^2}{s_w c_w}\right) \left(\frac{s}{s - m_Z^2}\right) F_{ij}^Z \\ \mathcal{F}_{ij}^R &= -F_{ij}^\gamma + \left(\frac{s_w^2}{s_w c_w}\right) \left(\frac{s}{s - m_Z^2}\right) F_{ij}^Z,\end{aligned}\tag{3}$$

where the subscripts, $i = 1, 2$ and $j = V, A$ refer to the structure of the form factor, and the superscripts refer to the helicity of the incoming electron.

We are now ready to discuss the helicity angle description of the complete event. As mentioned previously, in the limit of narrow width for the top and the W , the event can be considered as a succession of two-body decays. The first process we consider is the decay of the virtual γ, Z boson into the $t\bar{t}$ pair. Note that the intermediate vector boson receives twice the helicity of the initial electron, along the beam direction. This process can be described in the e^+e^- center-of-momentum frame by two angles, the polar angle θ and the azimuthal angle ϕ of the top with respect to the electron beam axis. Using the notation t_L and t_R to denote the helicities $h_t = -1/2$ and $h_t = +1/2$, we obtain the matrix elements

$$\begin{aligned}\mathcal{M}(e_L \bar{e}_R \rightarrow t_L \bar{t}_R) &= [\mathcal{F}_{1V}^L - \beta \mathcal{F}_{1A}^L + \mathcal{F}_{2V}^L] (1 + \cos \theta) e^{-i\phi} \\ \mathcal{M}(e_L \bar{e}_R \rightarrow t_R \bar{t}_L) &= [\mathcal{F}_{1V}^L + \beta \mathcal{F}_{1A}^L + \mathcal{F}_{2V}^L] (1 - \cos \theta) e^{-i\phi} \\ \mathcal{M}(e_L \bar{e}_R \rightarrow t_L \bar{t}_L) &= \gamma^{-1} [\mathcal{F}_{1V}^L + \gamma^2 (\mathcal{F}_{2V}^L + \beta \mathcal{F}_{2A}^L)] (\sin \theta) e^{-i\phi} \\ \mathcal{M}(e_L \bar{e}_R \rightarrow t_R \bar{t}_R) &= \gamma^{-1} [\mathcal{F}_{1V}^L + \gamma^2 (\mathcal{F}_{2V}^L - \beta \mathcal{F}_{2A}^L)] (\sin \theta) e^{-i\phi}\end{aligned}$$

$$\begin{aligned}
\mathcal{M}(e_R \bar{e}_L \rightarrow t_L \bar{t}_R) &= -[\mathcal{F}_{1V}^R - \beta \mathcal{F}_{1A}^R + \mathcal{F}_{2V}^R] (1 - \cos \theta) e^{i\phi} \\
\mathcal{M}(e_R \bar{e}_L \rightarrow t_R \bar{t}_L) &= -[\mathcal{F}_{1V}^R + \beta \mathcal{F}_{1A}^R + \mathcal{F}_{2V}^R] (1 + \cos \theta) e^{i\phi} \\
\mathcal{M}(e_R \bar{e}_L \rightarrow t_L \bar{t}_L) &= \gamma^{-1} [\mathcal{F}_{1V}^R + \gamma^2 (\mathcal{F}_{2V}^R + \beta \mathcal{F}_{2A}^R)] (\sin \theta) e^{i\phi} \\
\mathcal{M}(e_R \bar{e}_L \rightarrow t_R \bar{t}_R) &= \gamma^{-1} [\mathcal{F}_{1V}^R + \gamma^2 (\mathcal{F}_{2V}^R - \beta \mathcal{F}_{2A}^R)] (\sin \theta) e^{i\phi} ,
\end{aligned} \tag{4}$$

where we have removed a factor of ie^2 . Here, $\beta^2 = (1 - 4m_t^2/s)$ and $\gamma = \sqrt{s}/(2m_t)$. For longitudinally polarized beams the ϕ dependence will vanish.

The nice aspect of this helicity formalism is that the angular dependence of each of the amplitudes is determined, up to a relative phase, simply by angular momentum conservation. For instance, in the first matrix element the virtual vector boson has helicity -1 along the electron beam direction, the top has helicity -1/2, and the antitop has helicity +1/2. To conserve angular momentum the top must move in the electron direction and the antitop must move in the positron direction; hence the $(1 + \cos \theta)$ dependence. By measuring the angular distributions it is straightforward to extract the relative weights for each helicity combination, and thereby obtain the top quark form factors.

As an example, we plot in Fig. 1 the tree-level Standard Model production cross-section as a function of $\cos \theta$ for a top mass of 175 GeV and a collider energy of 400 GeV for polarized electron beams. We have also plotted the helicity subprocesses. Here we see that the e_L 's produce predominantly t_L 's highly peaked in the forward direction, while e_R 's produce predominantly t_R 's peaked in the forward direction. This can easily be understood in the limit of high energy, where the $SU(2)_L \times U(1)$

symmetry is restored and the squared matrix elements become

$$\begin{aligned}
|\mathcal{M}(e_L \bar{e}_R \rightarrow t_L \bar{t}_R)|^2 &= \left(\frac{1}{4s_w^2} + \frac{1}{12c_w^2} \right)^2 (1 + \cos \theta)^2 \sim 1.41 (1 + \cos \theta)^2 \\
|\mathcal{M}(e_L \bar{e}_R \rightarrow t_R \bar{t}_L)|^2 &= \left(\frac{1}{3c_w^2} \right)^2 (1 - \cos \theta)^2 \sim 0.19 (1 - \cos \theta)^2 \\
|\mathcal{M}(e_R \bar{e}_L \rightarrow t_R \bar{t}_L)|^2 &= \left(\frac{2}{3c_w^2} \right)^2 (1 + \cos \theta)^2 \sim 0.75 (1 + \cos \theta)^2 \\
|\mathcal{M}(e_R \bar{e}_L \rightarrow t_L \bar{t}_R)|^2 &= \left(\frac{1}{6c_w^2} \right)^2 (1 - \cos \theta)^2 \sim 0.05 (1 - \cos \theta)^2,
\end{aligned} \tag{5}$$

while the remaining matrix elements vanish. Thus, longitudinally polarized electrons are an excellent source of polarized top quarks.

The next stage in the event is the decay of the top $t \rightarrow bW^+$. This process is most conveniently described in the top rest frame obtained from the lab frame by rotating the axes $-\phi$, then $-\theta$, and then boosting in the direction opposite to the top momentum. The helicity angles in this frame are the polar angle χ_t and the azimuthal angle ψ_t of the W boson with respect to the top momentum axis. Using the notation (L, R, Z) to denote the W^+ helicities $(-1, +1, 0)$, we obtain the helicity amplitudes for the left-handed bottom quarks:

$$\begin{aligned}
\mathcal{M}(t_R \rightarrow b_L W_Z^+) &= w^{-1} [F_{1L}^W - \frac{1}{2} w^2 F_{2L}^W] (\cos \frac{\chi_t}{2}) e^{i\psi_t/2} \\
\mathcal{M}(t_L \rightarrow b_L W_Z^+) &= w^{-1} [F_{1L}^W - \frac{1}{2} w^2 F_{2L}^W] (\sin \frac{\chi_t}{2}) e^{-i\psi_t/2} \\
\mathcal{M}(t_R \rightarrow b_L W_L^+) &= \sqrt{2} [F_{1L}^W - \frac{1}{2} F_{2L}^W] (-\sin \frac{\chi_t}{2}) e^{i\psi_t/2} \\
\mathcal{M}(t_L \rightarrow b_L W_L^+) &= \sqrt{2} [F_{1L}^W - \frac{1}{2} F_{2L}^W] (\cos \frac{\chi_t}{2}) e^{-i\psi_t/2} \\
\mathcal{M}(t_L \rightarrow b_L W_R^+) &= \mathcal{M}(t_R \rightarrow b_L W_R^+) = 0,
\end{aligned} \tag{6}$$

where $w = m_W/m_t$, and we have dropped an overall factor of $igm_t(1 - w^2)^{1/2}/\sqrt{2}$.

The matrix elements for right-handed bottom quarks are obtained from these by replacing everywhere $L \leftrightarrow R$, $\psi_t \leftrightarrow -\psi_t$, and $\chi_t \leftrightarrow -\chi_t$.

As before, the angular dependence is exactly what is expected from angular momentum conservation in the decay of a spin-1/2 object. In addition, in the Standard Model in the limit $m_b = 0$ the top can only decay to b_L 's. Therefore, it must decay to W_Z^+ 's in the direction of the top quark spin, to W_L^+ 's in the direction opposite to the top quark spin, and it cannot decay to W_R^+ 's at all. In Fig. 2 we display this by plotting the $t_R \rightarrow bW^+$ decay distribution as a function of $\cos \chi_t$, while also plotting the helicity subprocesses. For increasing top mass the distribution becomes more sloped in the forward direction, indicating an increased partial width to W_Z^+ .

The antitop decay $\bar{t} \rightarrow \bar{b}W^-$ can be described in an analogous manner in the antitop rest-frame, obtained from the lab frame by rotating the axes $-\phi$, then $\pi - \theta$, and then boosting in the direction opposite to the antitop momentum. The helicity angles in this frame are the polar angles of the W^- , $\bar{\chi}_t$ and $\bar{\psi}_t$, with respect to the antitop momentum axis. If CP is a good symmetry we can obtain the matrix elements using

$$\mathcal{M}(t_h \rightarrow b_\rho W_\lambda^+) = \mathcal{M}(\bar{t}_{-h} \rightarrow \bar{b}_{-\rho} W_{-\lambda}^-), \quad (7)$$

while replacing $\chi_t \rightarrow \bar{\chi}_t$ and $\psi_t \rightarrow -\bar{\psi}_t$.

The final step in the decay chain is $W^+ \rightarrow \ell\nu$. We work in the W^+ rest frame obtained from the top rest frame by rotating the axes $-\psi_t$, then $-\chi_t$, and then boosting against the W^+ momentum. The helicity angles in this frame are the

polar angle χ and the azimuthal angle ψ of the charged lepton with respect to the W^+ momentum axis. For hadronic decays we can just replace ℓ^+ with the antiquark and ν with the quark. In the Standard model the W^+ can only decay to $\ell_R^+ \nu_L$ in the limit of massless leptons. The helicity amplitudes are

$$\begin{aligned}\mathcal{M}(W_R^+ \rightarrow \ell^+ \nu) &= \frac{1}{\sqrt{2}}(1 + \cos \chi) e^{i\psi} \\ \mathcal{M}(W_Z^+ \rightarrow \ell^+ \nu) &= \sin \chi \\ \mathcal{M}(W_L^+ \rightarrow \ell^+ \nu) &= \frac{1}{\sqrt{2}}(1 - \cos \chi) e^{-i\psi},\end{aligned}\tag{8}$$

where we have removed a factor of $igm_W/\sqrt{2}$. In Fig. 3 we plot the $\cos \chi$ distribution in the $W^+ \rightarrow \ell^+ \nu$ decay, along with helicity subprocesses, for W^+ produce in top decays. The zero at $\cos \chi = 1$ indicates the absence of right-handed W^+ 's.

Lastly, the decay $W^- \rightarrow \ell^- \bar{\nu}$ can be described in the W^- rest-frame, obtained from the top rest frame by rotating the axes $-\bar{\psi}_t$, then $-\bar{\chi}_t$, and then boosting against the W^- momentum. The helicity angles in this frame are the polar angles of the negatively-charged lepton, $\bar{\chi}$ and $\bar{\psi}$, with respect to the W^- momentum axis. We can obtain the helicity amplitudes from

$$\mathcal{M}(W_\lambda^+ \rightarrow \ell^+ \nu) = \mathcal{M}(W_{-\lambda}^- \rightarrow \ell^- \bar{\nu}),\tag{9}$$

while replacing $\chi \rightarrow \bar{\chi}$ and $\psi \rightarrow -\bar{\psi}$.

In practice, in order to optimize the analysis of the top quark form factors it is necessary to study the event in a multi-dimensional space of all these angles. The use of helicity angles makes it easy to discern which variables are most important for studying which form factors. For example, by cutting on the production angle

θ , while using a polarized electron beam, it is possible to obtain a sample of highly polarized top quarks. With these, one can study the decay form factors by looking at both the top decay angle χ_t and the W decay angle χ , in order to determine the helicities of the W 's. Perhaps the optimum technique would be to use all of the helicity angle information in a maximum likelihood fit[14]. In any case we now obtain the full tree-level correlation information of the event from

$$\left| \sum_{hh'\lambda\lambda'\rho\rho'} \mathcal{M}(e_\sigma \bar{e}_{\sigma'} \rightarrow t_h \bar{t}_{h'}) \mathcal{M}(t_h \rightarrow b_\rho W_\lambda^+) \mathcal{M}(W_\lambda^+ \rightarrow \ell^+ \nu) \right. \\ \left. \times \mathcal{M}(\bar{t}_{h'} \rightarrow \bar{b}_{\rho'} W_{\lambda'}^-) \mathcal{M}(W_{\lambda'}^- \rightarrow \ell^- \bar{\nu}) \right|^2 \quad (10)$$

for each initial-state helicity configuration.

3 The event at $\mathcal{O}(\alpha_s)$

In the narrow top-width approximation, in which the top quarks are treated as on-shell particles in the matrix elements, the $\mathcal{O}(\alpha_s)$ corrections can be unambiguously assigned to the $t\bar{t}$ production process, or to the t -decay or \bar{t} -decay processes. We have constructed a NLO Monte Carlo by separately building a generator for $t\bar{t}$ events with an extra gluon in the production, the t -decay, and the \bar{t} -decay processes, as well as for events with no extra visible gluon. To see how this is implemented it is easiest to temporarily ignore the angular correlations. Then the total differential cross section, $d\sigma_{\text{tot}}$, for the event $e^+e^- \rightarrow t\bar{t} + X \rightarrow b\ell^+\nu\bar{b}\ell^-\bar{\nu} + X$ is just the product of the $t\bar{t} + X$ differential production cross section, $d\sigma$, times the t and \bar{t}

decay distributions:

$$d\sigma_{\text{tot}} = d\sigma \frac{d\Gamma d\bar{\Gamma}}{\Gamma^2} . \quad (11)$$

To $\mathcal{O}(\alpha_s)$ this can be written

$$\begin{aligned} d\sigma_{\text{tot}}^{(0+1)} &= d\sigma^0 \frac{d\Gamma^0 d\bar{\Gamma}^0}{(\Gamma^0)^2} + d\sigma^1 \frac{d\Gamma^0 d\bar{\Gamma}^0}{(\Gamma^0)^2} + d\sigma^0 \frac{d\Gamma^1 d\bar{\Gamma}^0}{(\Gamma^0)^2} \\ &+ d\sigma^0 \frac{d\Gamma^0 d\bar{\Gamma}^1}{(\Gamma^0)^2} - \frac{2\Gamma^1}{\Gamma^0} d\sigma^0 \frac{d\Gamma^0 d\bar{\Gamma}^0}{(\Gamma^0)^2} , \end{aligned} \quad (12)$$

where the first term is the tree-level event, the second term includes $\mathcal{O}(\alpha_s)$ corrections to the $t\bar{t}$ production, the third and fourth terms contain the corrections to the t and the \bar{t} decay respectively, and the last term is the $\mathcal{O}(\alpha_s)$ correction to the widths in the denominator. Note that on integrating over the decay phase space, the last three terms cancel so that $\sigma_{\text{tot}}^{(0+1)} = \sigma^0 + \sigma^1$, *i.e.*, the integrated total event cross section is not affected by the corrections to the top quark decay, as required.

The $\mathcal{O}(\alpha_s)$ corrections to the production and decay can be separated into three pieces—the virtual (v), soft-gluon (s), and real-gluon (r) contributions:

$$\begin{aligned} d\sigma^1 &= d\sigma^v + d\sigma^s(x_0) + d\sigma^r(x_0) \\ d\Gamma^1 &= d\Gamma^v + d\Gamma^s(y_0, z_0) + d\Gamma^r(y_0, z_0) . \end{aligned} \quad (13)$$

The arbitrary distinction between “soft” and “real” gluons is implemented using artificial cutoffs x_0, y_0, z_0 , which we will describe more fully below. The real gluons are defined to be those produced above the cutoffs and are treated using the exact 3-body phase space. The soft gluons are those produced below the cutoffs and are integrated out analytically, leaving an effective 2-body phase space. Both the virtual and the soft contributions are infrared divergent, but their sum is infrared

finite. Thus, we can combine the virtual and soft contributions, and we can conveniently separate the full $\mathcal{O}(\alpha_s)$ cross section into the sum of four sub-event cross sections:

$$\begin{aligned} d\sigma_{\text{tot}}^{(0+1)} &= d\sigma_{\text{tot}}^{(v+s)}(x_0, y_0, z_0) + d\sigma^r(x_0) \frac{d\Gamma^0 d\bar{\Gamma}^0}{(\Gamma^0)^2} \\ &\quad + d\sigma^0 \frac{d\Gamma^r(y_0, z_0) d\bar{\Gamma}^0}{(\Gamma^0)^2} + d\sigma^0 \frac{d\Gamma^0 d\bar{\Gamma}^r(y_0, z_0)}{(\Gamma^0)^2}. \end{aligned} \quad (14)$$

The last three contributions have 7 final-state partons, containing a real gluon in the production, the t decay, or the \bar{t} decay respectively. Each of these terms is manifestly positive-definite. The first contribution has only 6 final-state partons and is given by the following sum:

$$\begin{aligned} d\sigma_{\text{tot}}^{(v+s)}(x_0, y_0, z_0) &= \left(1 - \frac{2\Gamma^1}{\Gamma^0}\right) d\sigma^0 \frac{d\Gamma^0 d\bar{\Gamma}^0}{(\Gamma^0)^2} + d\sigma^{(v+s)}(x_0) \frac{d\Gamma^0 d\bar{\Gamma}^0}{(\Gamma^0)^2} \\ &\quad + d\sigma^0 \frac{d\Gamma^{(v+s)}(y_0, z_0) d\bar{\Gamma}^0}{(\Gamma^0)^2} + d\sigma^0 \frac{d\Gamma^0 d\bar{\Gamma}^{(v+s)}(y_0, z_0)}{(\Gamma^0)^2}. \end{aligned} \quad (15)$$

This term may be negative for small values of the cutoffs. A separate Monte Carlo is used to generate events for each of the four terms in (14) with all angular correlations included.

We now elaborate on the infrared cancellations, as well as the separation into “soft” and “real” gluons, that are used in equation (14). The virtual corrections to the production and decay processes can be written as corrections to the form factors (1) and (2), with the understanding that they are only expanded to $\mathcal{O}(\alpha_s)$ in the squared amplitudes (10). Using dimensional regularization with $D = 4 - 2\epsilon$ we obtain the correction to the production form factors:

$$\delta F_{1V}^i = \frac{\alpha_s C_q}{2\pi} f_V^i (I_1 + I_2)$$

$$\begin{aligned}
\delta F_{1A}^i &= \frac{\alpha_s C_q}{2\pi} f_A^i (I_1 - I_2) \\
\delta F_{2V}^i &= \frac{\alpha_s C_q}{2\pi} f_V^i (2I_2)
\end{aligned} \tag{16}$$

where

$$\begin{aligned}
I_1 &= \left(\frac{4\pi\mu^2}{m_t^2} \right)^\epsilon \Gamma(1+\epsilon) \left\{ \frac{1}{\epsilon} \left[-1 - \frac{1+\beta^2}{2\beta} \left(\ln \frac{1-\beta}{1+\beta} + i\pi \right) \right] - 2 \right. \\
&\quad \left. + \frac{1+\beta^2}{2\beta} \left[\left(-\frac{3}{2} + \ln \frac{4\beta^2}{1-\beta^2} \right) \left(\ln \frac{1-\beta}{1+\beta} + i\pi \right) \right. \right. \\
&\quad \left. \left. + \frac{2\pi^2}{3} + 2\text{Li}_2\left(\frac{1-\beta}{1+\beta}\right) + \frac{1}{2} \left(\ln \frac{1-\beta}{1+\beta} \right)^2 \right] \right\} \\
I_2 &= \frac{1-\beta^2}{4\beta} \left[\ln \frac{1-\beta}{1+\beta} + i\pi \right],
\end{aligned} \tag{17}$$

$C_q = 4/3$, and $f_V^\gamma = \frac{2}{3}$, $f_A^\gamma = 0$, $f_V^Z = (\frac{1}{4} - \frac{2}{3}s_w^2)/s_w c_w$, and $f_A^Z = (-\frac{1}{4})/s_w c_w$ are the tree-level couplings. Also, we have used the Spence function $\text{Li}_2(z) = -\int_0^z dt \ln(1-t)/t$. This agrees with the previous results given in Ref. [9]. Note that the contribution from $\text{Re}I_1$ is proportional to the tree-level cross section, while $\text{Im}I_1$ does not contribute at $\mathcal{O}(\alpha_s)$.

For the real gluon corrections to $t\bar{t}$ production it is convenient to define the gluon phase space in terms of the variables

$$x = E_g/E_g^{\max}, \quad \Delta = (1 - \cos\theta_{tg}^*)/2, \tag{18}$$

where the maximum energy of the production gluon in the lab frame is $E_g^{\max} = \beta^2 \sqrt{s}/2$, and θ_{tg}^* is the angle between the gluon and top quark momenta in the $t\bar{t}$ rest frame. The full phase space is $0 < x < 1$, $0 < \Delta < 1$ with the soft gluon limit given by $x \rightarrow 0$. Integrating out the gluons in the region $x < x_0$, for small

x_0 , it is possible to absorb this soft-gluon contribution into the form factors (16) by replacing $I_1 \rightarrow I_1 + I_1^{(\text{soft})}$, with

$$\begin{aligned}
I_1^{(\text{soft})} = & \left(\frac{4\pi\mu^2}{m_t^2} \right)^\epsilon \Gamma(1+\epsilon) \left\{ \left(\frac{1}{\epsilon} - 2 \ln x_0 \right) \left[1 + \frac{1+\beta^2}{2\beta} \ln \frac{1-\beta}{1+\beta} \right] \right. \\
& + \ln \frac{1-\beta^2}{4\beta^4} - \frac{1}{\beta} \ln \frac{1-\beta}{1+\beta} \\
& + \frac{1+\beta^2}{2\beta} \left[-\ln \beta^2 \ln \frac{1-\beta}{1+\beta} - \frac{\pi^2}{3} \right. \\
& \left. \left. + 2\text{Li}_2\left(\frac{1-\beta}{1+\beta}\right) + \frac{1}{2} \left(\ln \frac{1-\beta}{1+\beta} \right)^2 \right] \right\}. \tag{19}
\end{aligned}$$

The sum of the virtual and soft contributions $\text{Re}(I_1 + I_1^{(\text{soft})})$ is now IR finite. The “real” gluons with $x > x_0$ are treated using exact kinematics. The matrix elements can be written in terms of helicity amplitudes as in section 2. We leave the details of this to the appendix A.

The virtual corrections to the top decay form factors at $\mathcal{O}(\alpha_s)$ are

$$\begin{aligned}
\delta F_{1L}^W = & \frac{\alpha_s C_q}{2\pi} \left(\frac{4\pi\mu^2}{m_t^2} \right)^\epsilon \Gamma(1+\epsilon) \left\{ -\frac{1}{2\epsilon^2} + \frac{1}{\epsilon} \left[-\frac{5}{4} + \ln(1-w^2) \right] \right. \\
& - 3 - \left(\ln(1-w^2) \right)^2 \\
& \left. + \frac{3}{2} \ln(1-w^2) - \text{Li}_2(w^2) \right\} \tag{20} \\
\delta F_{2L}^W = & \frac{\alpha_s C_q}{2\pi} w^{-2} \ln(1-w^2).
\end{aligned}$$

For the phase space of the real gluon in top decay we use the variables

$$y = E_g/E_g^{\text{max}}, \quad z = (1 - \cos \theta_{bg}^*)/2, \tag{21}$$

where the maximum energy of the decay gluon in the top rest frame is $E_g^{\text{max}} = (m_t/2)(1-w^2)$, and θ_{bg}^* is the angle between the gluon and bottom quark momenta

in the bW rest frame. The gluon becomes soft in the limit $y \rightarrow 0$ and collinear in the limit $z \rightarrow 0$. Integrating out the soft and collinear gluons for which $y < y_0$ and/or $z < z_0$, for small y_0, z_0 , we can absorb these contributions into the form factor F_{1L}^W . They contribute

$$\begin{aligned}
\delta F_{1L}^{W(\text{soft})} = & \frac{\alpha_s C_q}{2\pi} \left(\frac{4\pi\mu^2}{m_t^2} \right)^\epsilon \Gamma(1+\epsilon) \left\{ \frac{1}{2\epsilon^2} + \frac{1}{\epsilon} \left[\frac{5}{4} - \ln(1-w^2) \right] \right. \\
& + 4 + \frac{5-3w^2}{8(1-w^2)} + \left(\ln(1-w^2) \right)^2 \\
& - \frac{5}{2} \ln(1-w^2) + \text{Li}_2(1-w^2) \\
& - \frac{w^2(2-3w^2)}{4(1-w^2)^2} \ln w^2 - \frac{\pi^2}{2} \\
& \left. - (1 + \ln x_0)(1 + \ln z_0) + \frac{1}{4} \ln z_0 \right\}, \tag{22}
\end{aligned}$$

so that the sum of the virtual and soft-gluon contributions $\delta F_{1L}^W + \delta F_{1L}^{W(\text{soft})}$ is IR finite. As in the production process, the “real” gluons with $y > y_0$ and $z > z_0$ are treated using exact kinematics. The helicity amplitudes are given in the appendix B.

It is useful at this stage to describe the Monte Carlo more fully. It is written in the C++ programming language and contains a separate event-generator class for each of the four sub-channel processes in equation (14). Each of these sub-channel generators are in turn derived from a single tree-level generator which produces the helicity angles of the event with the exact tree-level distributions. The sub-channel generators then produce the relevant gluon kinematic variables, prepare the particle four-vectors, and give the event a weight. The production-gluon class generates the gluon variables (18) with a soft gluon distribution, while the decay-gluon classes

generate the gluon variables (21) with a soft and collinear gluon distribution. This results in a very efficient Monte Carlo for each of the four sub-channels.

The relative contribution from the four sub-channels depends on the artificial IR cutoffs (x_0, y_0, z_0) . The choice of values for these parameters is determined by several considerations. First, the analytic integrations of the soft gluons contained in (19) and (22) are valid up to terms linear in the cutoffs, so they should be kept as small as possible. In addition, they should lie below any physical cutoff, determined by the detector energy resolution or the jet definition. However, for very small cutoffs the contribution containing the virtual and soft gluons will become very large and negative, and there will be large cancellations between it and the other sub-channels. Thus, the cutoffs should not be too small or else the numerical errors will become prohibitive. Luckily, this last constraint turns out to be not too restrictive for our Monte Carlo. For each plot in the next two sections we have checked that the results do not change significantly for smaller values of the cutoffs. As a final test of our confidence, we have checked that our Monte Carlo reproduces the $\mathcal{O}(\alpha_s)$ production[9] and decay distributions[11] of previous analyses.

Our Monte Carlo also allows the inclusion of width effects by generating Breit-Wigner resonance distributions for the tops and the W 's. In addition, the kinematic effects of the bottom quark mass can be included. Momentum conservation is maintained by shifting the energies of the final-state particles, while keeping the helicity angles and the gluon kinematic variables (18) and (21) fixed. This procedure should be good to $\mathcal{O}(\Gamma_t/m_t)$ except very near threshold. Note, however, that the matrix elements, and hence the event weights, are always computed in the

zero-width and $m_b = 0$ limits. Finally, initial state radiation (ISR) can be included by generating electron and positron momentum fractions z with the distribution function given by Fadin and Kuraev[15]

$$D_e(z) = \hat{\beta}/2(1-z)^{\hat{\beta}/2-1} (1 + 3\hat{\beta}/8) - \hat{\beta}(1+z)/4, \quad (23)$$

where $\hat{\beta} = (2\alpha/\pi)(\ln s/m_e^2 - 1)$.

It must be noted that the narrow-width approximation is necessary for the NLO analysis of this section. As a consequence, the Monte Carlo does not include the effects of interference between gluons emitted in the production and gluons emitted in the decay. These perturbative effects have been studied in the soft-gluon limit in Refs. [16]. Typically, the interference is only important for gluons with energy $E_g \leq \Gamma_t$. However, it should be considered in a complete analysis. In addition, because the final-state bottom quarks do carry bare color, there will be some nonperturbative information connecting them in the form of soft hadrons[17]. We have neglected this effect here.

4 The effects of radiated gluons

In this section we will study the top quark mass reconstruction and helicity angle distributions at next-to-leading order. We do this by starting with an ideal event situation—no ISR, an ideal 4π detector, perfect partonic-level particle identification. In the subsequent section we will make each of these factors more realistic experimentally. The purpose here is to develop our intuition by isolating the purely theoretical QCD effects at NLO. If we assume that both bottom quarks and W 's

are identified and signed and that there is 4π detector coverage, then the only ambiguity is in where to put the gluon. Does it belong to the t , to the \bar{t} , or to neither?

Here, we will make this assignment of the real gluon in analogy with the typical jet-clustering algorithm used at e^+e^- colliders. Defining the quantities $\mu^2 = (p_b + p_g)^2$ and $\bar{\mu}^2 = (\bar{p}_b + p_g)^2$, we make the assignment:

$$\begin{aligned}
\text{if } \mu < \bar{\mu} \text{ and } \mu < \mu_{cut} &\Rightarrow \text{gluon belongs to } t \text{ decay} \\
&\quad (p_t = p_g + p_b + p_{W^+} , \bar{p}_t = \bar{p}_b + p_{W^-}) , \\
\text{if } \bar{\mu} < \mu \text{ and } \bar{\mu} < \mu_{cut} &\Rightarrow \text{gluon belongs to } \bar{t} \text{ decay} \\
&\quad (p_t = p_b + p_{W^+} , \bar{p}_t = p_g + \bar{p}_b + p_{W^-}) , \\
\text{else} &\Rightarrow \text{gluon belongs to production} \\
&\quad (p_t = p_b + p_{W^+} , \bar{p}_t = \bar{p}_b + p_{W^-}) .
\end{aligned} \tag{24}$$

In the limit $m_b = 0$, we recognize μ_{cut} as an infrared cutoff on both the collinear and soft gluons in the event. In fact, we can consider the decay gluons to be clustered with the bottom quarks[18] using the standard jet resolution parameter $y_{cut} = \mu_{cut}^2/s$. By varying μ_{cut} we change the fraction of events with gluons that are not combined with the b or \bar{b} , and thus are considered to be part of the production process. This fraction is plotted in Fig. 4 as a function of the center-of-mass energy for various values of μ_{cut} . At this fixed order in perturbation theory, the fraction can be greater than one, indicating that a resummation of the large logarithms in y_{cut} or μ_{cut}^2/m_t^2 is necessary. As in all of our plots we use a standard top mass of 175 GeV and $\alpha_s = 0.12$.

We now consider the top quark mass distribution at $\sqrt{s} = 400$ GeV. Using

the algorithm (24), each event produces two mass values $m^2 = p_t^2$ and $\bar{m}^2 = \bar{p}_t^2$, which are binned independently. To see most clearly how the radiation affects this distribution, we plot it in Fig. 5(a) in the strict zero top-width limit for values of $\mu_{cut} = 5, 10, 20$, and ∞ GeV. Note that for $\mu_{cut} = \infty$, all of the observed gluons are assigned either to top decay or antitop decay, and none to the production. The Monte Carlo cutoffs used are $x_0 = 0.02$, $y_0 = 0.005$, and $z_0 = 0.01$. The δ -function spike in the central bin arises from those events in which the top momentum is determined correctly from its true decay products. The excess below the δ -function corresponds to events where a decay gluon is assigned incorrectly and is not included in the top momentum reconstruction. These missed-gluon events become less likely as μ_{cut} increases, but even for $\mu_{cut} = \infty$ there is a remnant of events where the gluon gets assigned to the wrong-charge top quark. The excess above the δ -function corresponds to events where an extra gluon is incorrectly included in a top momentum reconstruction. This region has two separate contributions, from mis-assigned decay gluons and from mis-assigned production gluons. Both of these increase with increasing μ_{cut} , with the production gluons adding a second bump for larger values of this parameter. The deficits in the distribution directly on each side of the spike are due to the artificial cutoffs x_0 , y_0 , and z_0 .

The δ -function peak in this distribution is an artifact of the zero-width approximation. Turning on the Breit-Wigner resonance for the top quark effectively smears over the δ -function and results in a well-defined IR-finite mass distribution. In Fig. 5(b) we plot this distribution using the same values of μ_{cut} as before. For comparison, we also plot the initial Breit-Wigner distribution. We now choose the

Monte Carlo cutoffs to be $x_0 = 0.002$, $y_0 = 0.0013$, and $z_0 = 0.0028$. These cutoffs ensure that all production gluons with $E_g > 100$ MeV and all decay gluons with $\mu, \bar{\mu} > 5$ GeV are treated with exact kinematics. The distributions do not change significantly for smaller x_0, y_0, z_0 . For $\mu_{cut} = 5$ GeV we see that the mass distribution is severely distorted, while for higher values of μ_{cut} it quickly regains an approximate Breit-Wigner shape, with a small decrease in the peak and an increase in the tail regions. We cannot take the $\mu_{cut} = 5$ GeV curve too seriously, however, because for small values of μ_{cut} we are probing the collinear-gluon region of the decay phase space. On the other hand, the effects of soft-gluon singularities are inconsequential, because soft gluons have $E_g \approx 0$ and do not affect the mass measurement. For $\mu_{cut} \gtrsim 20$ GeV these perturbative mass distributions should be reliable. Fig. 5(b) suggests that perhaps the best approach to mass reconstruction at $\sqrt{s} = 400$ GeV is to treat each extra gluon as coming from decay, combining it with whichever top quark has the smaller value of μ . This is because 400 GeV is still not too far from threshold, where real gluon radiation in the production process is suppressed.

At higher energies the situation changes dramatically. In Fig. 6 we plot the mass distributions at $\sqrt{s} = 1$ TeV for $\mu_{cut} = 5, 20, 80$ and ∞ GeV. At this center-of-mass energy we choose $x_0 = .0001$ so that production gluons with $E_g > 100$ MeV are treated with exact kinematics. The best resonant peak occurs for $\mu_{cut} \sim 20$ GeV. At this high energy there is substantial collinear radiation in the $t\bar{t}$ production process, so that for larger values of μ_{cut} an extra gluon is usually included with one of the tops, resulting in a too-large mass reconstruction. These curves are

suggestive of the degradation that will occur at this energy, but a resummation of the collinear gluons would be necessary to obtain an exact prediction. Certainly, determining the top mass at $\sqrt{s} = 1$ TeV would be more difficult than at lower energies.

We now turn to the top production angle distribution. For the remainder of this section, we work in the strict zero-width and $m_b = 0$ limits. The production angle distribution has been studied before at $\mathcal{O}(\alpha_s)$ for the pure $t\bar{t}$ production process in [9]. Here we include the effects of radiative corrections in both production and decay of the top quarks. Although the corrections to the decay process do not affect this distribution for perfectly reconstructed $t\bar{t}$ events, they are significant when reconstruction ambiguities are considered. For a given value of μ_{cut} we can use the algorithm (24) to reconstruct each event and then bin with respect to the top and antitop production variables $\cos\theta$ and $-\cos\bar{\theta}$. The tree-level production angle distributions for $m_t = 175$ GeV and $\sqrt{s} = 400$ GeV were shown in Fig. 1. In Fig. 7 we plot the deviations from the tree-level distribution for several different values of μ_{cut} for left- and right-handed electron beams. We also plot the pure production corrections[9], which assume perfect gluon discrimination and event reconstruction. For both electron polarizations the $\mathcal{O}(\alpha_s)$ corrections tend to increase the slope of the distribution with production angle. However, the treatment of the radiative gluon can have a significant effect on this correction. For a left-polarized electron beam, using smaller values of μ_{cut} , the correction even changes sign. This is shown further in Table 1, where we give the $\mathcal{O}(\alpha_s)$ corrections to the forward-backward asymmetry of the top quarks for the different values of μ_{cut} .

In Fig. 8 we examine the effects of the gluon ambiguity on the decay angle of the top quark to the W^+ boson, χ_t . Using the algorithm (24) the W^+ boson is reconstructed correctly, but the observed momentum of the top quark, and therefore the observed value of χ_t , is affected by the treatment of the radiative gluon. In Fig. 8 we plot the fraction of observed values of $\cos \chi_t$ falling in each 0.1-width bin for events with true values of $\cos \chi_t$ between -0.1 and 0.0. For small μ_{cut} the reconstructed values of $\cos \chi_t$ tend to be larger than the true values. The missed gluons in the decay lead to an underestimate of the top momentum, which results in an underestimate of the angle between the W^+ and the top momenta after boosting to the top rest frame. As in the previous examples, the most accurate reconstruction occurs for large μ_{cut} .

5 More detailed analysis of top mass reconstruction

In this section we re-examine the top mass distribution with more realistic experimental assumptions. The neutrinos are undetected and the quark jets are indistinguishable. We include the effects of initial-state radiation, and we impose simple lab-frame angular cuts to approximate the effects of the detector. We also examine the effects of parton energy smearing due to the detector resolution. However, we stop short of including final-state hadronization. This analysis is strictly at the partonic level.

We will consider the reconstruction of the top quarks in both the lepton+jets

mode and the all-jets mode. We require that all of the visible partons must satisfy $|\cos \theta_{lab}| < 0.9$, and we cluster[18] the colored partons into jets using the jet resolution parameter $y_{cut} = \mu_{cut}^2/s$ with $\mu_{cut} = 20$ GeV. We do not consider the effects of b -tagging, treating all hadronic jets as indistinguishable. We then use a simple algorithm for $t\bar{t}$ event reconstruction in each mode. Certainly, these methods can be improved and optimized, but they will be sufficient for our purposes.

In the all-jets mode we require that there be ≥ 6 jets after the cuts and the clustering. We then choose two pairs of jets to form the W 's by minimizing the quantity

$$\left[(p_1 + p_2)^2 - m_W^2\right]^2 + \left[(p_3 + p_4)^2 - m_W^2\right]^2 \quad (25)$$

over all combinations of jets. We then combine one or more of the remaining jets with each of the W 's, so as to minimize the mass difference between the resulting top quarks.

In the lepton+jets mode we require that there be a charged lepton and ≥ 4 jets after the cuts and clustering. The neutrino four-momentum is defined to be equal to the missing momentum in the event, $p_\nu = p_{total} - \sum p_{visible}$, with the additional requirement that

$$|m(\ell\nu) - m_W| < 10 \text{ GeV} . \quad (26)$$

Then a pair of jets is chosen to form the second W boson by minimizing $|(p_1 + p_2)^2 - m_W^2|$ over all of the jets. Finally, we combine at least one of the remaining jets with each of the W 's, so as to minimize the mass difference between the resulting top quarks.

We begin our study by including the initial-state radiation, but omitting the final-state energy smearing. The mass distributions for the all-jet channel and for the lepton+jets channel are shown in Figs. 9(a) and 9(b), respectively, for $m_t = 175$ GeV and $\sqrt{s} = 400$ GeV. For comparison we also show the original Breit-Wigner distributions, as well as the mass reconstructions at tree-level for both channels. The $\mathcal{O}(\alpha_s)$ distributions exhibit a moderate degradation as compared to tree-level and also as compared to the $\mu_{cut} = \infty$ curve of Fig. 5(b) from the previous section. This is due to the additional complexity in clustering the radiated gluon and reconstructing the event. Naturally, these effects are more serious in the all-jet channel. In the lepton+jets channel there can also be errors in the neutrino reconstruction due to initial-state radiation. This is the source of the enhanced tail at higher masses. Of the all-jet events, 41% survive the cuts and are identified as a 6-jet event, while 4% are identified with 7 jets. Of the lepton+jet events, 35% survive the cuts and are identified with 4 jets, while 7% are identified with 5 jets.

In Fig. 10 we show the same distributions with the final-state partons smeared in energy to approximate the effects of the detector energy resolution. The hadronic and leptonic final-state partons are gaussian-smeared with the parameters used in the JLC study[19]:

$$\frac{\sigma_E^{had}}{E} = \frac{0.4}{\sqrt{E}}, \quad \frac{\sigma_E^{lep}}{E} = \frac{0.15}{\sqrt{E}}, \quad (27)$$

where E is in GeV. The smearing has no effect on the efficiency in the all-jets mode, but it does reduce the efficiencies in the lepton+jet modes to 22% (4 jets) and 4% (5 jets). This is because, when the jet energies are smeared, the reconstructed neutrino is less likely to meet the constraint (26). From Fig. 10 we conclude that

the major contribution to the error on the top mass distribution will probably come from the detector energy resolution, making a direct width measurement virtually impossible. The gluon radiation also contributes a significant amount to the widening of the peak, especially in the all-jets reconstruction channel. As we have shown in this paper, this QCD radiative contribution is directly calculable in perturbation theory.

The plots in this section are representative of the accuracy that may be obtainable in a direct mass measurement, although certainly the reconstruction algorithm can be better optimized, and b -tagging would be very useful in this regard. As for the angular distributions, we would expect the detector resolution effects to be less serious because detector angular resolution is usually better than energy resolution. However, the reconstruction errors may still be significant for these distributions.

6 Conclusions

As in any hard scattering process, the $e^+e^- \rightarrow t\bar{t}$ event is certainly more complex than the basic tree-level parton cross section would indicate. The first step to a more realistic treatment should include QCD radiation in the final state. This requires the correct handling of radiation both in the $\gamma^* \rightarrow t\bar{t}$ production process and in the $t \rightarrow bW^+$ decay process. In this paper we have shown how to include this radiation to $\mathcal{O}(\alpha_s)$ and have constructed a Monte Carlo generator to study these effects. In doing this we have made strong use of the helicity angle formalism, which is the most natural for investigating the properties of the top quark.

The treatment of the $t\bar{t}$ event at $\mathcal{O}(\alpha_s)$ introduces reconstruction ambiguities whenever there is real gluon radiation. We have shown how this can alter the top mass distribution and the angular distributions. By including the Breit-Wigner resonance shape for the top quark, we obtain an infrared finite correction to the mass distribution. The major effect of the QCD radiation is to degrade the peak, with practically no shift in the position of the maximum. For energies not too far above the $t\bar{t}$ threshold, most of the gluon radiation occurs during the decay of the quarks; however, at higher energies the radiation off the tops during the production phase becomes more important.

Acknowledgements

I wish to thank Michael Peskin for collaboration in the early stages of this project. I would also like to thank him and Timothy Barklow for many useful suggestions and comments.

Appendices

A $e^+e^- \rightarrow t\bar{t}g$ production amplitudes

The real radiative corrections to $t\bar{t}$ production and decay can be given by helicity amplitudes, with only minor complications due to the three-body final state. We can describe the $t\bar{t}g$ production event configuration in the lab frame in terms of five variables. Two of these are the energy fractions $x_i = 2E_i/\sqrt{s}$ of the top and the

gluon, which are in turn determined by the variables of equation (18). These fix all of the lab-frame energies and angles within the $t\bar{t}g$ -plane. Two more variables are just the polar angle θ and azimuthal angle ϕ of the top quark with respect to the electron beam axis. The final variable that we need is the angle ϕ_g between the e^+e^-t -plane and the $t\bar{t}g$ -plane, rotated around the top momentum axis. Note that the rotation by ϕ_g around the top quark momentum axis also rotates its decay products. This completely determines the event kinematics.

For longitudinally polarized electrons, the intermediate photon- Z state will be an eigenstate of spin along the beam axis. However, it is more convenient to work in a basis where the vector boson is a spin eigenstate along the top momentum direction. Labeling these eigenstates by γ_λ , we can expand the matrix elements in terms of amplitudes in the new basis, which are now independent of the variables ϕ , θ , and ϕ_g :

$$\begin{aligned}
\mathcal{M}(e_L\bar{e}_R \rightarrow t\bar{t}g) &= e^{-i\phi} \left\{ \right. \\
&\quad \left[\mathcal{F}_{1L}^L \mathcal{M}(L; \gamma_L \rightarrow t\bar{t}g) + \mathcal{F}_{1R}^L \mathcal{M}(R; \gamma_L \rightarrow t\bar{t}g) \right] \frac{1}{\sqrt{2}} (1 + \cos \theta) e^{-i\phi_g} \\
&\quad + \left[\mathcal{F}_{1L}^L \mathcal{M}(L; \gamma_R \rightarrow t\bar{t}g) + \mathcal{F}_{1R}^L \mathcal{M}(R; \gamma_R \rightarrow t\bar{t}g) \right] \frac{1}{\sqrt{2}} (1 - \cos \theta) e^{i\phi_g} \\
&\quad \left. + \left[\mathcal{F}_{1L}^L \mathcal{M}(L; \gamma_Z \rightarrow t\bar{t}g) + \mathcal{F}_{1R}^L \mathcal{M}(R; \gamma_Z \rightarrow t\bar{t}g) \right] \sin \theta \right\} \\
\mathcal{M}(e_R\bar{e}_L \rightarrow t\bar{t}g) &= e^{i\phi} \left\{ \right. \\
&\quad - \left[\mathcal{F}_{1L}^R \mathcal{M}(L; \gamma_L \rightarrow t\bar{t}g) + \mathcal{F}_{1R}^R \mathcal{M}(R; \gamma_L \rightarrow t\bar{t}g) \right] \frac{1}{\sqrt{2}} (1 - \cos \theta) e^{-i\phi_g} \\
&\quad - \left[\mathcal{F}_{1L}^R \mathcal{M}(L; \gamma_R \rightarrow t\bar{t}g) + \mathcal{F}_{1R}^R \mathcal{M}(R; \gamma_R \rightarrow t\bar{t}g) \right] \frac{1}{\sqrt{2}} (1 + \cos \theta) e^{i\phi_g} \\
&\quad \left. + \left[\mathcal{F}_{1L}^R \mathcal{M}(L; \gamma_Z \rightarrow t\bar{t}g) + \mathcal{F}_{1R}^R \mathcal{M}(R; \gamma_Z \rightarrow t\bar{t}g) \right] \sin \theta \right\} .
\end{aligned} \tag{28}$$

We have also separated the pieces arising from the left-handed and right-handed currents. The form factors $\mathcal{F}_{1R}^i = \mathcal{F}_{1V}^i + \mathcal{F}_{1A}^i$ and $\mathcal{F}_{1L}^i = \mathcal{F}_{1V}^i - \mathcal{F}_{1A}^i$ are obtained from equation (3) evaluated at tree level.

The matrix elements in equation (28) with left-handed currents are:

$$\begin{aligned}
\mathcal{M}(L; \gamma_L \rightarrow t_L \bar{t}_L g_L) &= -A_{+-} \sin \frac{\theta_{tg}}{2} \cos \frac{\theta_{tg}}{2} \cos \frac{\theta_{t\bar{t}}}{2} (x_t \beta_t + (1 - x_t)) \\
\mathcal{M}(L; \gamma_R \rightarrow t_L \bar{t}_L g_L) &= A_{+-} \sin^2 \frac{\theta_{tg}}{2} \sin \frac{\theta_{t\bar{t}}}{2} (1 - x_t) \\
\mathcal{M}(L; \gamma_Z \rightarrow t_L \bar{t}_L g_L) &= -\frac{A_{+-}}{\sqrt{2}} \sin \frac{\theta_{tg}}{2} (x_t \beta_t \cos \frac{\theta_{tg}}{2} \sin \frac{\theta_{t\bar{t}}}{2} + (1 - x_t) \sin \frac{\theta_{t\bar{t}} - \theta_{tg}}{2}) \\
\mathcal{M}(L; \gamma_L \rightarrow t_L \bar{t}_L g_R) &= A_{+-} \sin \frac{\theta_{tg}}{2} (x_t \beta_t \cos \frac{\theta_{tg}}{2} \cos \frac{\theta_{t\bar{t}}}{2} + (1 - \bar{x}_t) \cos \frac{\theta_{t\bar{t}} + \theta_{tg}}{2}) \\
\mathcal{M}(L; \gamma_R \rightarrow t_L \bar{t}_L g_R) &= 0 \\
\mathcal{M}(L; \gamma_Z \rightarrow t_L \bar{t}_L g_R) &= \frac{A_{+-}}{\sqrt{2}} \cos \frac{\theta_{tg}}{2} (x_t \beta_t \sin \frac{\theta_{tg}}{2} \sin \frac{\theta_{t\bar{t}}}{2} + (1 - \bar{x}_t) \cos \frac{\theta_{t\bar{t}} + \theta_{tg}}{2}) \\
\mathcal{M}(L; \gamma_L \rightarrow t_R \bar{t}_L g_L) &= -A_{--} \cos^2 \frac{\theta_{tg}}{2} \cos \frac{\theta_{t\bar{t}}}{2} (1 - x_t) \\
\mathcal{M}(L; \gamma_R \rightarrow t_R \bar{t}_L g_L) &= -A_{--} \sin \frac{\theta_{tg}}{2} \cos \frac{\theta_{tg}}{2} \sin \frac{\theta_{t\bar{t}}}{2} (x_t \beta_t - (1 - x_t)) \\
\mathcal{M}(L; \gamma_Z \rightarrow t_R \bar{t}_L g_L) &= -\frac{A_{--}}{\sqrt{2}} \cos \frac{\theta_{tg}}{2} (x_t \beta_t \sin \frac{\theta_{tg}}{2} \cos \frac{\theta_{t\bar{t}}}{2} + (1 - x_t) \sin \frac{\theta_{t\bar{t}} - \theta_{tg}}{2}) \\
\mathcal{M}(L; \gamma_L \rightarrow t_R \bar{t}_L g_R) &= 0 \\
\mathcal{M}(L; \gamma_R \rightarrow t_R \bar{t}_L g_R) &= A_{--} \cos \frac{\theta_{tg}}{2} (x_t \beta_t \sin \frac{\theta_{tg}}{2} \sin \frac{\theta_{t\bar{t}}}{2} + (1 - \bar{x}_t) \cos \frac{\theta_{t\bar{t}} + \theta_{tg}}{2}) \\
\mathcal{M}(L; \gamma_Z \rightarrow t_R \bar{t}_L g_R) &= \frac{A_{--}}{\sqrt{2}} \sin \frac{\theta_{tg}}{2} (x_t \beta_t \cos \frac{\theta_{tg}}{2} \cos \frac{\theta_{t\bar{t}}}{2} + (1 - \bar{x}_t) \cos \frac{\theta_{t\bar{t}} + \theta_{tg}}{2}) \\
\mathcal{M}(L; \gamma_L \rightarrow t_L \bar{t}_R g_L) &= -A_{++} \sin \frac{\theta_{tg}}{2} \cos \frac{\theta_{tg}}{2} \sin \frac{\theta_{t\bar{t}}}{2} (x_t \beta_t + (1 - x_t)) \\
\mathcal{M}(L; \gamma_R \rightarrow t_L \bar{t}_R g_L) &= -A_{++} \sin^2 \frac{\theta_{tg}}{2} \cos \frac{\theta_{t\bar{t}}}{2} (1 - x_t) \\
\mathcal{M}(L; \gamma_Z \rightarrow t_L \bar{t}_R g_L) &= \frac{A_{++}}{\sqrt{2}} \sin \frac{\theta_{tg}}{2} (x_t \beta_t \cos \frac{\theta_{tg}}{2} \cos \frac{\theta_{t\bar{t}}}{2} + (1 - x_t) \cos \frac{\theta_{t\bar{t}} - \theta_{tg}}{2})
\end{aligned} \tag{29}$$

$$\begin{aligned}
\mathcal{M}(L; \gamma_L \rightarrow t_L \bar{t}_R g_R) &= A_{++} \sin \frac{\theta_{tg}}{2} (x_t \beta_t \cos \frac{\theta_{tg}}{2} \sin \frac{\theta_{t\bar{t}}}{2} + (1 - \bar{x}_t) \sin \frac{\theta_{t\bar{t}} + \theta_{tg}}{2}) \\
\mathcal{M}(L; \gamma_R \rightarrow t_L \bar{t}_R g_R) &= 0 \\
\mathcal{M}(L; \gamma_Z \rightarrow t_L \bar{t}_R g_R) &= -\frac{A_{++}}{\sqrt{2}} \cos \frac{\theta_{tg}}{2} (x_t \beta_t \sin \frac{\theta_{tg}}{2} \cos \frac{\theta_{t\bar{t}}}{2} - (1 - \bar{x}_t) \sin \frac{\theta_{t\bar{t}} + \theta_{tg}}{2}) \\
\mathcal{M}(L; \gamma_L \rightarrow t_R \bar{t}_R g_L) &= -A_{-+} \cos^2 \frac{\theta_{tg}}{2} \sin \frac{\theta_{t\bar{t}}}{2} (1 - x_t) \\
\mathcal{M}(L; \gamma_R \rightarrow t_R \bar{t}_R g_L) &= A_{-+} \sin \frac{\theta_{tg}}{2} \cos \frac{\theta_{tg}}{2} \cos \frac{\theta_{t\bar{t}}}{2} (x_t \beta_t - (1 - x_t)) \\
\mathcal{M}(L; \gamma_Z \rightarrow t_R \bar{t}_R g_L) &= -\frac{A_{-+}}{\sqrt{2}} \cos \frac{\theta_{tg}}{2} (x_t \beta_t \sin \frac{\theta_{tg}}{2} \sin \frac{\theta_{t\bar{t}}}{2} - (1 - x_t) \cos \frac{\theta_{t\bar{t}} - \theta_{tg}}{2}) \\
\mathcal{M}(L; \gamma_L \rightarrow t_R \bar{t}_R g_R) &= 0 \\
\mathcal{M}(L; \gamma_R \rightarrow t_R \bar{t}_R g_R) &= -A_{-+} \cos \frac{\theta_{tg}}{2} (x_t \beta_t \sin \frac{\theta_{tg}}{2} \cos \frac{\theta_{t\bar{t}}}{2} - (1 - \bar{x}_t) \sin \frac{\theta_{t\bar{t}} + \theta_{tg}}{2}) \\
\mathcal{M}(L; \gamma_Z \rightarrow t_R \bar{t}_R g_R) &= \frac{A_{-+}}{\sqrt{2}} \sin \frac{\theta_{tg}}{2} (x_t \beta_t \cos \frac{\theta_{tg}}{2} \sin \frac{\theta_{t\bar{t}}}{2} + (1 - \bar{x}_t) \sin \frac{\theta_{t\bar{t}} + \theta_{tg}}{2}) ,
\end{aligned}$$

where

$$A_{\pm\pm} = -ie^2 g_s T^a \frac{x_g [x_t \bar{x}_t (1 \pm \beta_t)(1 \pm \bar{\beta}_t)]^{1/2}}{\sqrt{s}(1 - x_t)(1 - \bar{x}_t)} , \quad (30)$$

with $\text{Tr}(T^a T^b) = \delta^{ab}/2$. The remaining matrix elements can be obtained from

$$\begin{aligned}
\mathcal{M}(L, R; \gamma_\lambda \rightarrow t_L \bar{t}_L g_\sigma) &= -(-1)^\lambda \mathcal{M}(R, L; \gamma_{-\lambda} \rightarrow t_R \bar{t}_R g_{-\sigma}) \\
\mathcal{M}(L, R; \gamma_\lambda \rightarrow t_L \bar{t}_R g_\sigma) &= (-1)^\lambda \mathcal{M}(R, L; \gamma_{-\lambda} \rightarrow t_R \bar{t}_L g_{-\sigma}) .
\end{aligned} \quad (31)$$

In terms of the variables in equation (18) the energy fractions are

$$\begin{aligned}
x_g &= x\beta^2 \\
x_t &= 1 - \frac{x_g}{2} + x_g \left(\Delta - \frac{1}{2} \right) \left(\frac{\beta^2 - x_g}{1 - x_g} \right)^{1/2} \\
\bar{x}_t &= 2 - x_g - x_t
\end{aligned} \quad (32)$$

Here $\beta^2 = 1 - 4m_t^2/s$ is the tree level velocity of the top quarks, while the velocities

of the t and \bar{t} in the presence of the radiated gluon are

$$\begin{aligned}\beta_t^2 &= 1 - \frac{4m_t^2}{x_t^2 s} \\ \bar{\beta}_t^2 &= 1 - \frac{4m_t^2}{\bar{x}_t^2 s} .\end{aligned}\tag{33}$$

The lab-frame angles are obtained from

$$\begin{aligned}\cos \theta_{t\bar{t}} &= \frac{1}{x_t \beta_t \bar{x}_t \bar{\beta}_t} \left[x_g - x_t - \bar{x}_t + x_t \bar{x}_t + \frac{4m_t^2}{s} \right] \\ \cos \theta_{tg} &= \frac{1}{x_t \beta_t x_g} [\bar{x}_t - x_t - x_g + x_t x_g] .\end{aligned}\tag{34}$$

B $t \rightarrow bW^+g$ decay amplitudes

The helicity amplitudes for top decay with a radiated gluon can be calculated in an analogous manner to the production calculation in appendix A. We describe the decay configuration in the top rest frame in terms of five variables. Two of these are the energy fractions $x_i = 2E_i/m_t$ of the W^+ and the gluon. These energies are determined by the variables of equation (21), and they fix all the energies and angles within the bW^+g decay plane. Two more variables are the polar angle χ_t and azimuthal angle ψ_t of the W^+ with respect to the top momentum boost axis. The final variable is the angle ϕ_g between the plane given by the top boost axis and the W^+ momentum and the bW^+g -plane, rotated around the W^+ momentum. This rotation by ϕ_g also rotates the W^+ decay products.

We can make explicit the dependence of the matrix elements on the variables χ_t , ψ_t , and ϕ_g if we expand the top helicity eigenstates t_h onto a basis of spin

eigenstates along the W^+ momentum direction. Labeling these states as t'_h we obtain the relations:

$$\begin{aligned}
\mathcal{M}(t_L \rightarrow bW^+g) &= e^{-i\psi_t/2} \left[\mathcal{M}(t'_R \rightarrow bW^+g) \sin \frac{\chi_t}{2} e^{i\phi_g/2} + \mathcal{M}(t'_L \rightarrow bW^+g) \cos \frac{\chi_t}{2} e^{-i\phi_g/2} \right] \\
\mathcal{M}(t_R \rightarrow bW^+g) &= e^{i\psi_t/2} \left[\mathcal{M}(t'_R \rightarrow bW^+g) \cos \frac{\chi_t}{2} e^{i\phi_g/2} - \mathcal{M}(t'_L \rightarrow bW^+g) \sin \frac{\chi_t}{2} e^{-i\phi_g/2} \right].
\end{aligned} \tag{35}$$

The helicity amplitudes in this basis are

$$\begin{aligned}
\mathcal{M}(t'_R \rightarrow b_L W_R g_L) &= -\frac{2}{\sqrt{\zeta} x_g} \left(x_g \cos \frac{\theta_{Wg}}{2} + x_b \cos \frac{\theta_{Wb}}{2} \cos \frac{\theta_{Wg} + \theta_{Wb}}{2} \right) \\
\mathcal{M}(t'_L \rightarrow b_L W_R g_L) &= 0 \\
\mathcal{M}(t'_R \rightarrow b_L W_L g_L) &= 0 \\
\mathcal{M}(t'_L \rightarrow b_L W_L g_L) &= \frac{2}{\sqrt{\zeta} x_g} \left(-x_g \sin \frac{\theta_{Wg}}{2} + x_b \sin \frac{\theta_{Wb}}{2} \cos \frac{\theta_{Wg} + \theta_{Wb}}{2} \right) \\
\mathcal{M}(t'_R \rightarrow b_L W_Z g_L) &= \frac{x_W(1 + \beta_W)}{w\sqrt{2\zeta} x_g} \left(-x_g \sin \frac{\theta_{Wg}}{2} + x_b \sin \frac{\theta_{Wb}}{2} \cos \frac{\theta_{Wg} + \theta_{Wb}}{2} \right) \\
\mathcal{M}(t'_L \rightarrow b_L W_Z g_L) &= -\frac{x_W(1 - \beta_W)}{w\sqrt{2\zeta} x_g} \left(x_g \cos \frac{\theta_{Wg}}{2} + x_b \cos \frac{\theta_{Wb}}{2} \cos \frac{\theta_{Wg} + \theta_{Wb}}{2} \right) \\
\mathcal{M}(t'_R \rightarrow b_L W_R g_R) &= \sqrt{x_b} \cos \frac{\theta_{Wb}}{2} \left(2\sqrt{\frac{x_b}{\zeta x_g}} \cos \frac{\theta_{Wg} + \theta_{Wb}}{2} - \sin \theta_{Wg} \right) \\
\mathcal{M}(t'_L \rightarrow b_L W_R g_R) &= -\sqrt{x_b} \cos \frac{\theta_{Wb}}{2} (1 - \cos \theta_{Wg}) \\
\mathcal{M}(t'_R \rightarrow b_L W_L g_R) &= -\sqrt{x_b} \sin \frac{\theta_{Wb}}{2} (1 + \cos \theta_{Wg}) \\
\mathcal{M}(t'_L \rightarrow b_L W_L g_R) &= -\sqrt{x_b} \sin \frac{\theta_{Wb}}{2} \left(2\sqrt{\frac{x_b}{\zeta x_g}} \cos \frac{\theta_{Wg} + \theta_{Wb}}{2} + \sin \theta_{Wg} \right) \\
\mathcal{M}(t'_R \rightarrow b_L W_Z g_R) &= \frac{x_W \sqrt{x_b}}{2\sqrt{2}w} \left[(1 + \beta_W) \sin \frac{\theta_{Wb}}{2} \left(-2\sqrt{\frac{x_b}{\zeta x_g}} \cos \frac{\theta_{Wg} + \theta_{Wb}}{2} + \sin \theta_{Wg} \right) \right.
\end{aligned} \tag{36}$$

$$\begin{aligned}
& + (1 - \beta_W) \cos \frac{\theta_{Wb}}{2} (1 + \cos \theta_{Wg}) \Big] \\
\mathcal{M}(t'_L \rightarrow b_L W_{ZgR}) &= \frac{x_W \sqrt{x_b}}{2\sqrt{2}w} \left[(1 - \beta_W) \cos \frac{\theta_{Wb}}{2} \left(2\sqrt{\frac{x_b}{\zeta x_g}} \cos \frac{\theta_{Wg} + \theta_{Wb}}{2} + \sin \theta_{Wg} \right) \right. \\
& \left. + (1 + \beta_W) \sin \frac{\theta_{Wb}}{2} (1 - \cos \theta_{Wg}) \right] .
\end{aligned}$$

where we have dropped a factor of $-iT^a g_s g / \sqrt{2}$. In terms of the variables of (21) the energy fractions are

$$\begin{aligned}
x_g &= y(1 - w^2) \\
x_W &= 1 + w^2 - z \frac{x_g(1 - w^2 - x_g)}{1 - x_g} \\
x_b &= 2 - x_g - x_W ,
\end{aligned} \tag{37}$$

and we have also introduced the variable $\zeta = 2p_b \cdot p_g / m_t^2 = 1 + w^2 - x_W$. The velocity of the W^+ is given by

$$\beta_W^2 = 1 - \frac{4w^2}{x_W^2} . \tag{38}$$

The angles in the top rest frame are obtained from

$$\begin{aligned}
\cos \theta_{Wb} &= \frac{1}{x_W \beta_W x_b} [x_g - x_W - x_b + x_W x_b + 2w^2] \\
\cos \theta_{Wg} &= \frac{1}{x_W \beta_W x_g} [x_b - x_W - x_g + x_W x_g + 2w^2] .
\end{aligned} \tag{39}$$

The amplitudes for \bar{t} decay in its rest frame can be obtained from these by simply using

$$\mathcal{M}(t_h \rightarrow b_\rho W_\lambda^+ g_\sigma) = \mathcal{M}(\bar{t}_{-h} \rightarrow \bar{b}_{-\rho} W_{-\lambda}^- g_{-\sigma}) , \tag{40}$$

while replacing all of the energies and polar angles of t decay with the corresponding variables of \bar{t} decay and replacing the azimuthal angles by $\psi_t \rightarrow -\bar{\psi}_t$ and $\phi_g \rightarrow -\phi_g$.

References

- [1] F. Abe et al. (CDF Collaboration), preprint FERMILAB-PUB-95/022-E (1995), hep-ex-9503002.
- [2] S. Abachi et al. (D0 Collaboration), preprint FERMILAB-PUB-95/028-E (1995), hep-ex-9503003.
- [3] J. Erler and P. Langacker, preprint UPR-0632T, hep-ph-9411203 (1994).
- [4] R. Chivukula, E. Simmons, J. Terning, *Phys. Lett.* **B331** (1994) 383.
- [5] C. Hill and S. Parke, *Phys. Rev.* **D49** (1994) 4454.
E. Eichten and K. Lane, *Phys. Lett.* **B327** (1994) 129.
- [6] P. Zerwas, in *Physics and Experiments with Linear Colliders*, R. Orava, P. Eerola, and M. Nordberg, eds. (World Scientific, Singapore, 1992).
J. Kuhn, in *Physics and Experiments with Linear e^+e^- Colliders*, F. Harris, S. Olsen, S. Pakvasa, and X. Tata, eds. (World Scientific, Singapore, 1993).
- [7] M. Jezabek, preprint TTP94-09, hep-ph-9406411 (1994).
- [8] V. Fadin and V. Khoze, *JETP Lett.* **46** (1987) 525 and *Sov. J. Nucl. Phys.* **48** (1988) 309; M. Strassler and M. Peskin, *Phys. Rev.* **D43** (1991) 1500; See also [6] and [7] and references therein.
- [9] J. Jersák, E. Laermann, and P. Zerwas, *Phys. Rev.* **D25** (1982) 1218.
- [10] J. Korner, A. Pilaftsis, M. Tung *Z. Phys.* **C63** (1994) 575.

- [11] M. Jezabek and J. Kuhn, *Phys. Lett.* **B329** (1994) 317.
- [12] The effects of this ambiguity from gluon radiation in top quark decay at hadronic colliders has been studied before by S. Mrenna and C.-P. Yuan, *Phys. Rev.* **D46** (1992) 1007.
- [13] G. Kane, G. Ladinsky, and C.-P. Yuan, *Phys. Rev.* **D45** (1992) 124.
- [14] T. Barklow and C. Schmidt, preprint SCIPP-94/22, (1994).
- [15] V. Fadin and E. Kuraev, *Sov. J. Nucl. Phys.* **41** (1985) 466.
- [16] G. Jikia, *Phys. Lett.* **B257** (1991) 196;
V. Khoze, W. Stirling, and L. Orr, *Nucl. Phys.* **B378** (1992) 413;
Y. Dokshitzer, V. Khoze, L. Orr, and W. Stirling, *Nucl. Phys.* **B403** (1993) 65.
- [17] V. Khoze and T. Sjostrand, *Phys. Lett.* **B328** (1994) 466.
- [18] The jet-clustering used here is labeled algorithm E in S. Bethke et al., *Nucl. Phys.* **B370** (1992) 310. At the order to which we are working the differences between algorithms is not significant.
- [19] JLC Group, *JLC-I*, Tsukuba, Japan, KEK Report 92-16, (1992).

	μ_{cut} (in GeV)				production
	5	10	20	∞	only
e_L^-	-2.8	-0.7	+1.2	+3.3	+3.2
e_R^-	+4.2	+3.6	+3.0	+2.5	+2.9

Table 1: Percentage $\mathcal{O}(\alpha_s)$ corrections to the top quark forward-backward asymmetry for $m_t = 175$ GeV and $\sqrt{s} = 400$ GeV with polarized electrons. The first four columns are using the reconstruction algorithm (24), while the last column gives the corrections from production only, assuming exact event reconstruction.

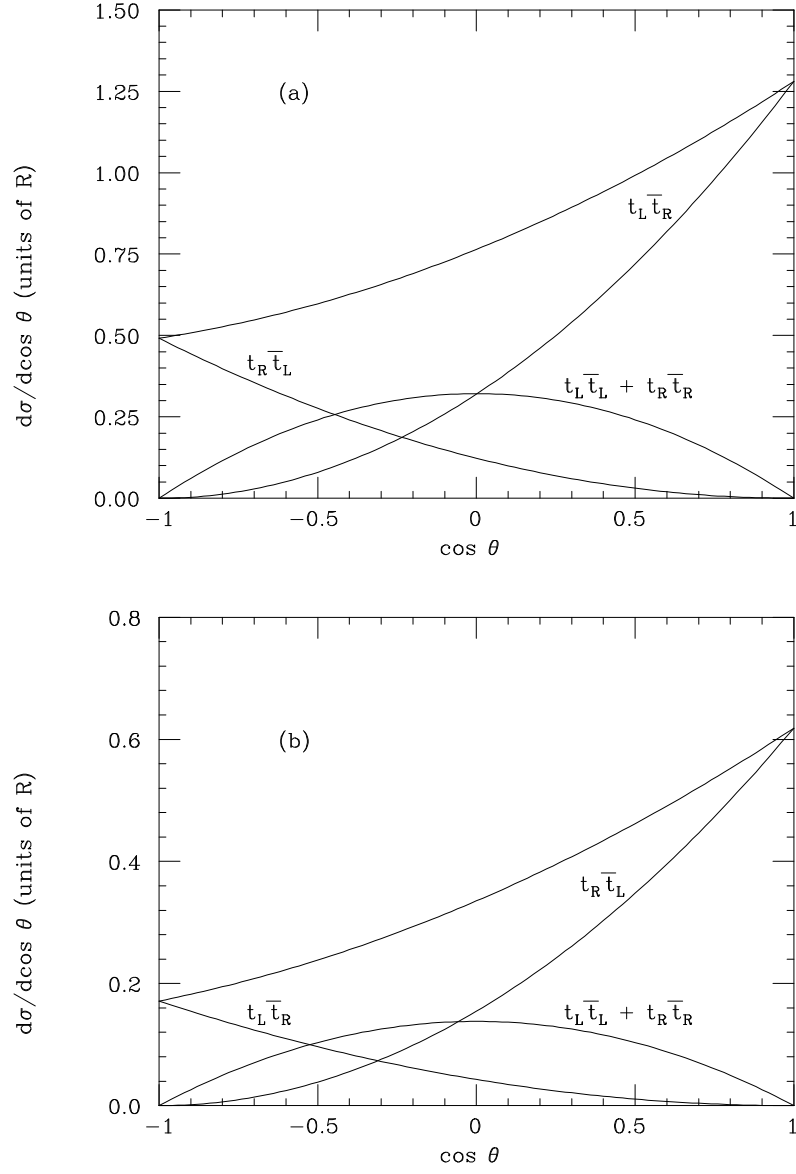


Fig. 1: $e^+e^- \rightarrow t\bar{t}$ cross section for (a) left-polarized electrons and (b) right-polarized electrons.

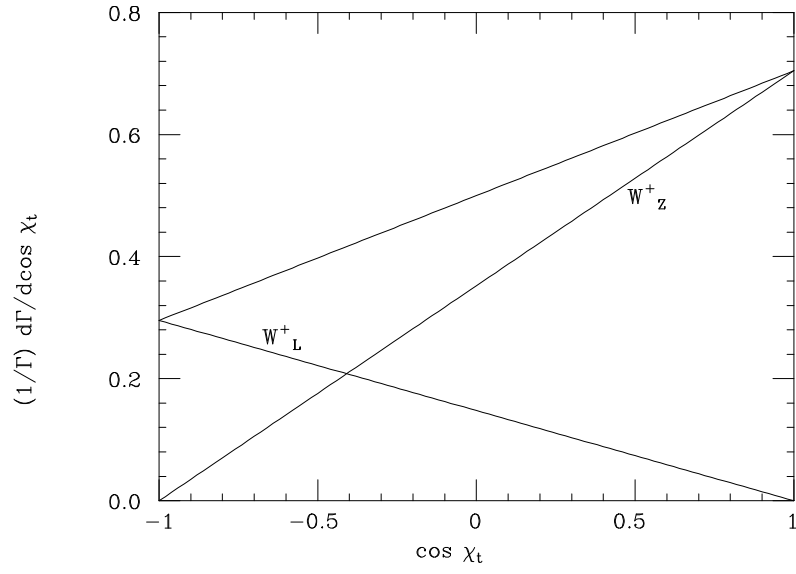


Fig. 2: Polar angle dependence of W^+ from decay of right-handed top quark.

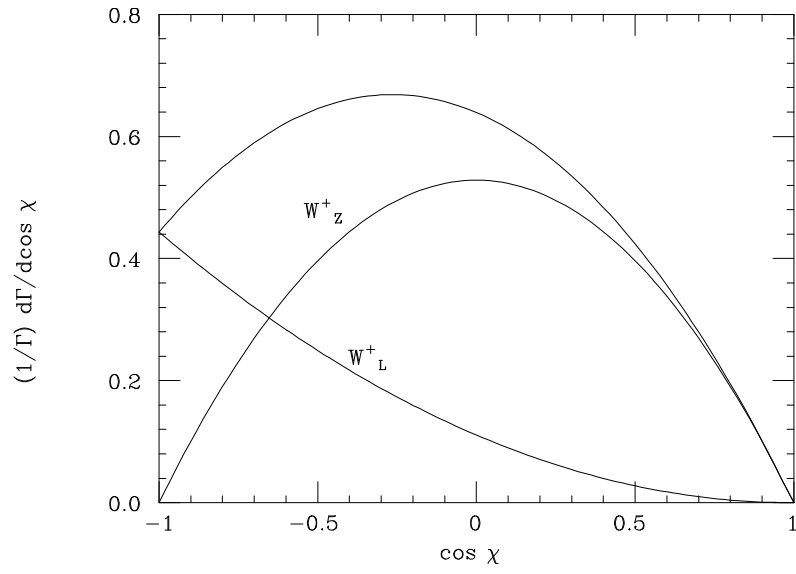


Fig 3: Polar angle dependence of ℓ^+ from decay of W^+ in a $t\bar{t}$ event.

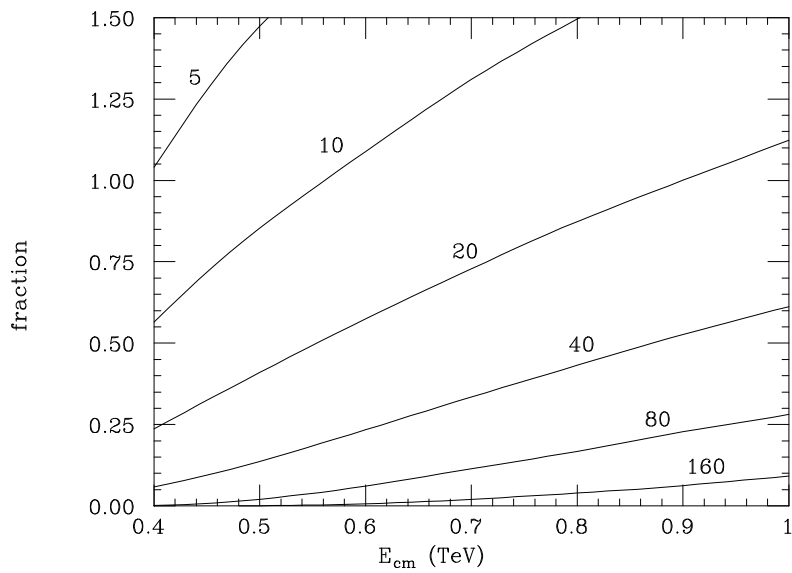


Fig. 4: Fraction of events containing a production gluon as a function of \sqrt{s} . The curves are, from top to bottom, for $\mu_{\text{cut}} = 5, 10, 20, 40, 80$, and 160 GeV.

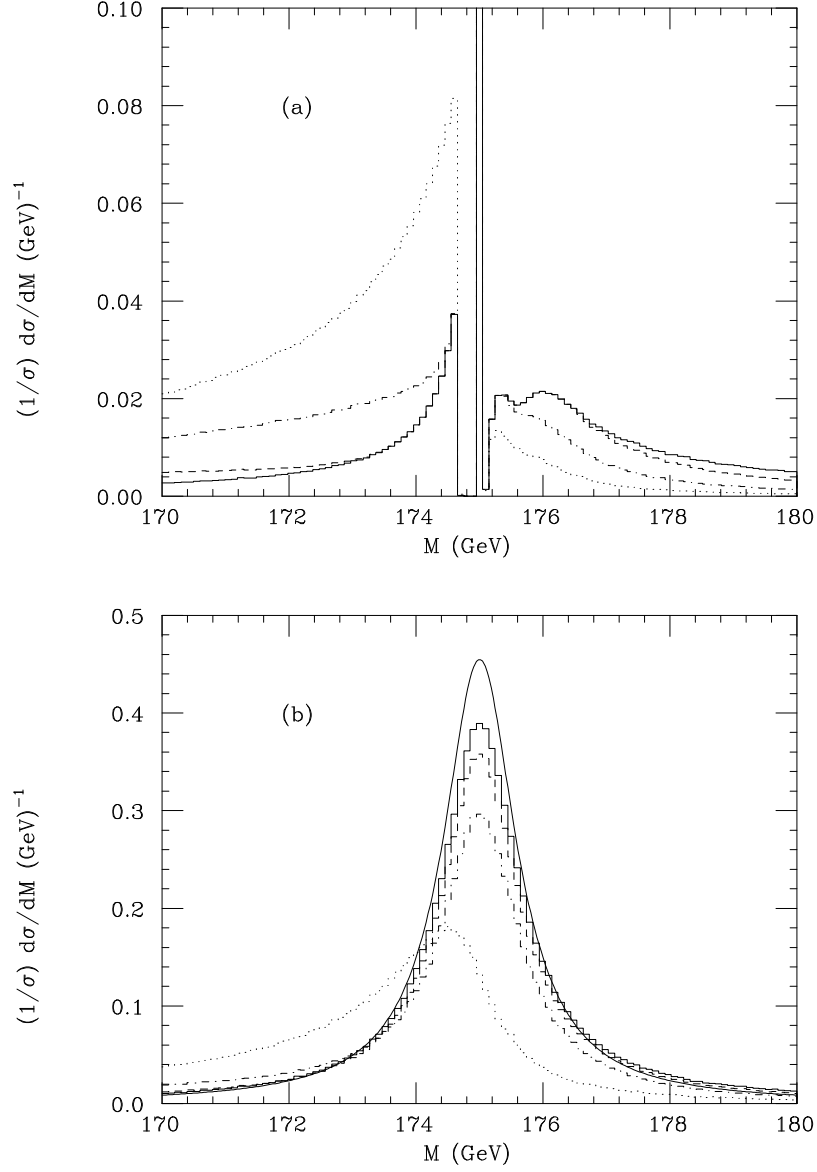


Fig. 5: Top mass reconstruction distributions for $\sqrt{s} = 400$ GeV (a) in the zero-width limit and (b) with an initial Breit-Wigner resonance distribution. The histograms are for $\mu_{cut} = 5$ GeV (dots), 10 GeV (dotdash), 20 GeV (dashes), and ∞ (solid). The smooth curve in (b) is the original Breit-Wigner distribution.

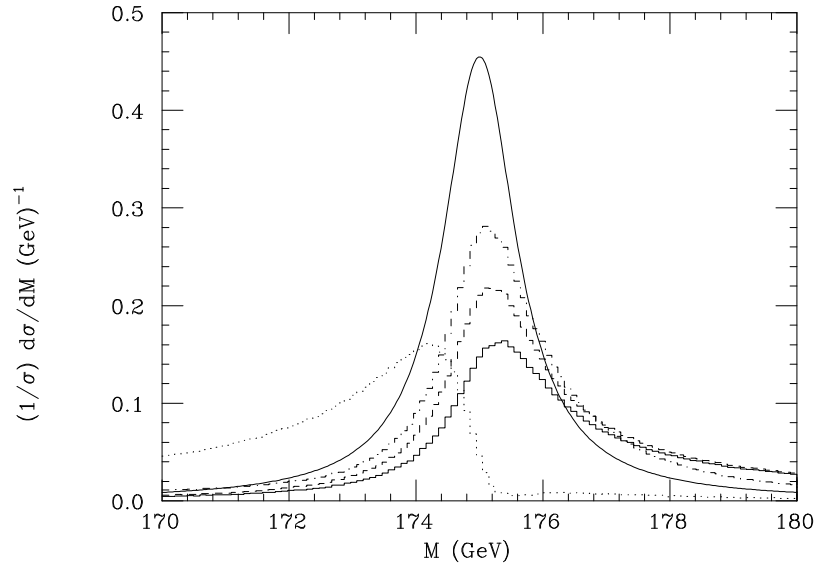


Fig. 6: Top mass reconstruction distributions for $\sqrt{s} = 1$ TeV with an initial Breit-Wigner resonance distribution. The histograms are for $\mu_{cut} = 5$ GeV (dots), 20 GeV (dotdash), 80 GeV (dashes), and ∞ (solid). The smooth curve is the original Breit-Wigner distribution.

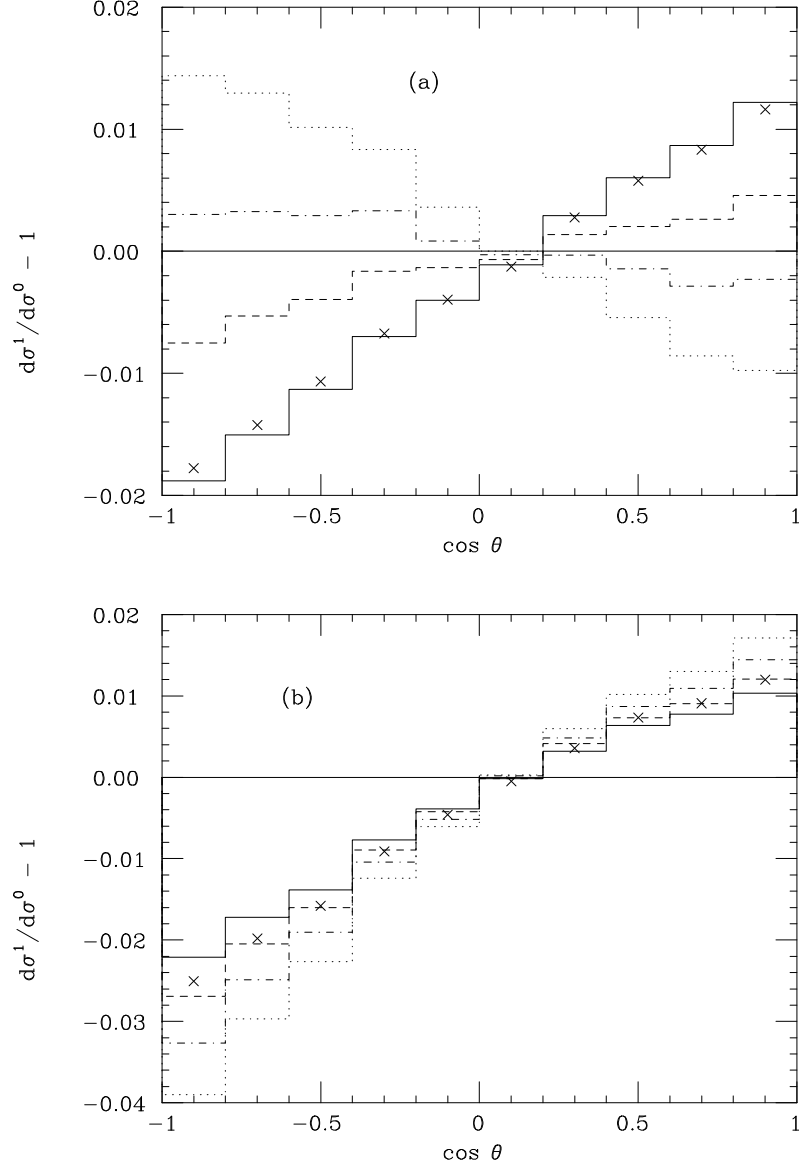


Fig. 7: The $\mathcal{O}(\alpha_s)$ corrections to the top quark polar angle distributions for $\sqrt{s} = 400$ GeV with (a) left-polarized electrons and (b) right-polarized electrons. The histograms are for $\mu_{cut} = 5$ GeV (dots), 10 GeV (dotdash), 20 GeV (dashes), and ∞ (solid), while the points plotted with the symbol \times are the pure production corrections.

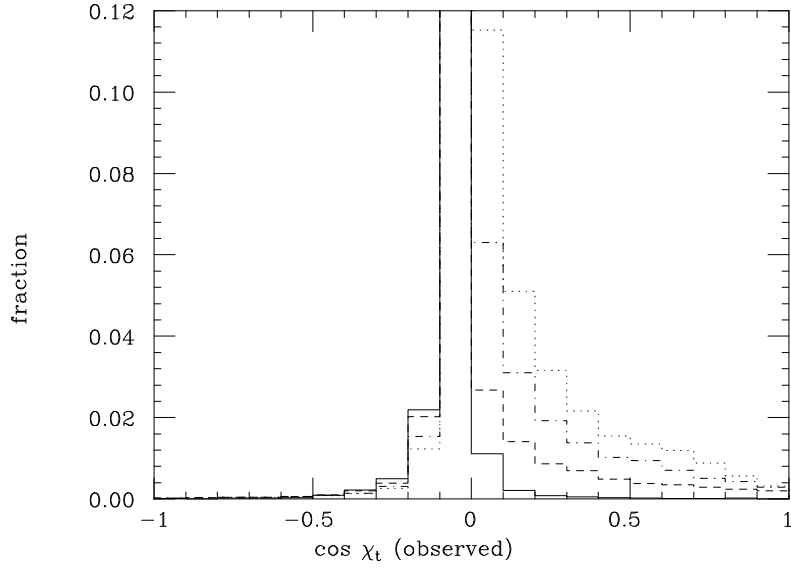


Fig. 8: Distribution of observed $\cos \chi_t$ for events with true $\cos \chi_t$ between -0.1 and 0.0. The histograms are for $\mu_{cut} = 5$ GeV (dots), 10 GeV (dotdash), 20 GeV (dashes), and ∞ (solid).

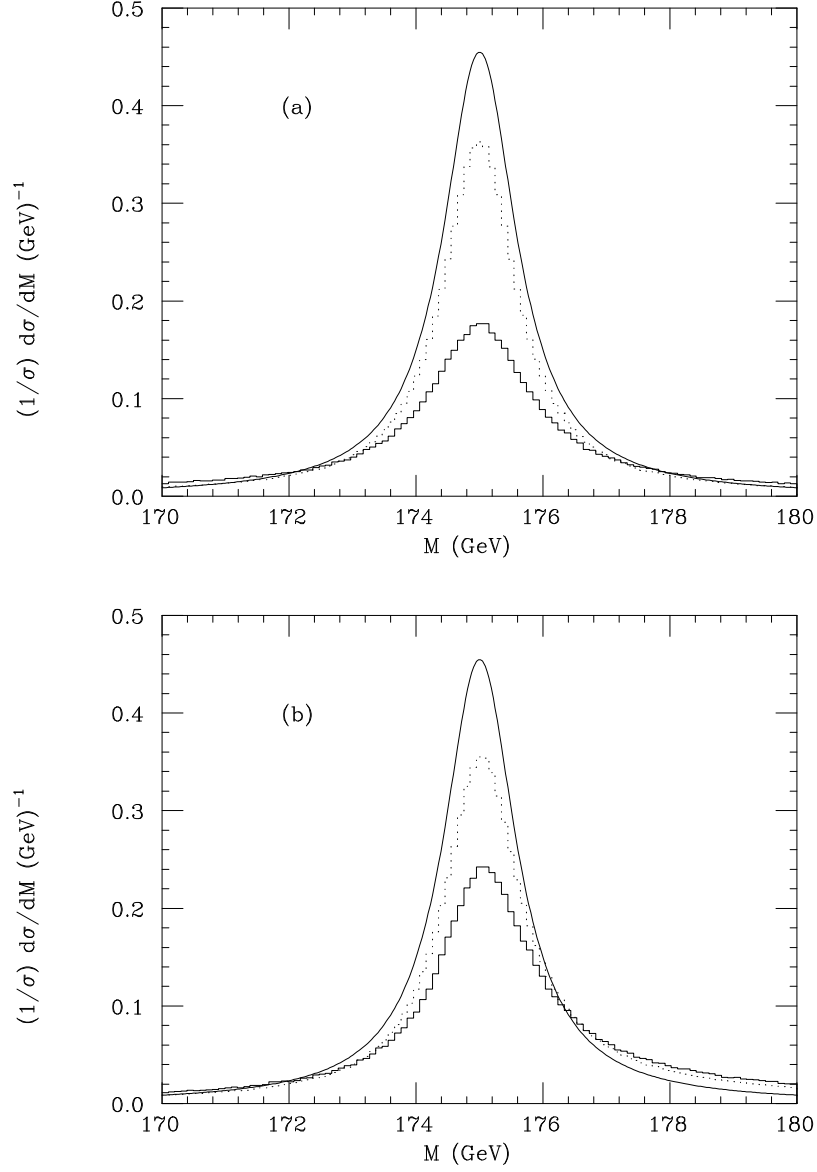


Fig. 9: Top mass reconstruction distributions without energy smearing of the final-state partons for $\sqrt{s} = 400$ GeV (a) in the all-jet mode and (b) in the lepton+jets mode. In both plots the dotted histogram is at tree-level, the solid histogram is at $\mathcal{O}(\alpha_s)$, and the smooth curve is the original Breit-Wigner distribution.

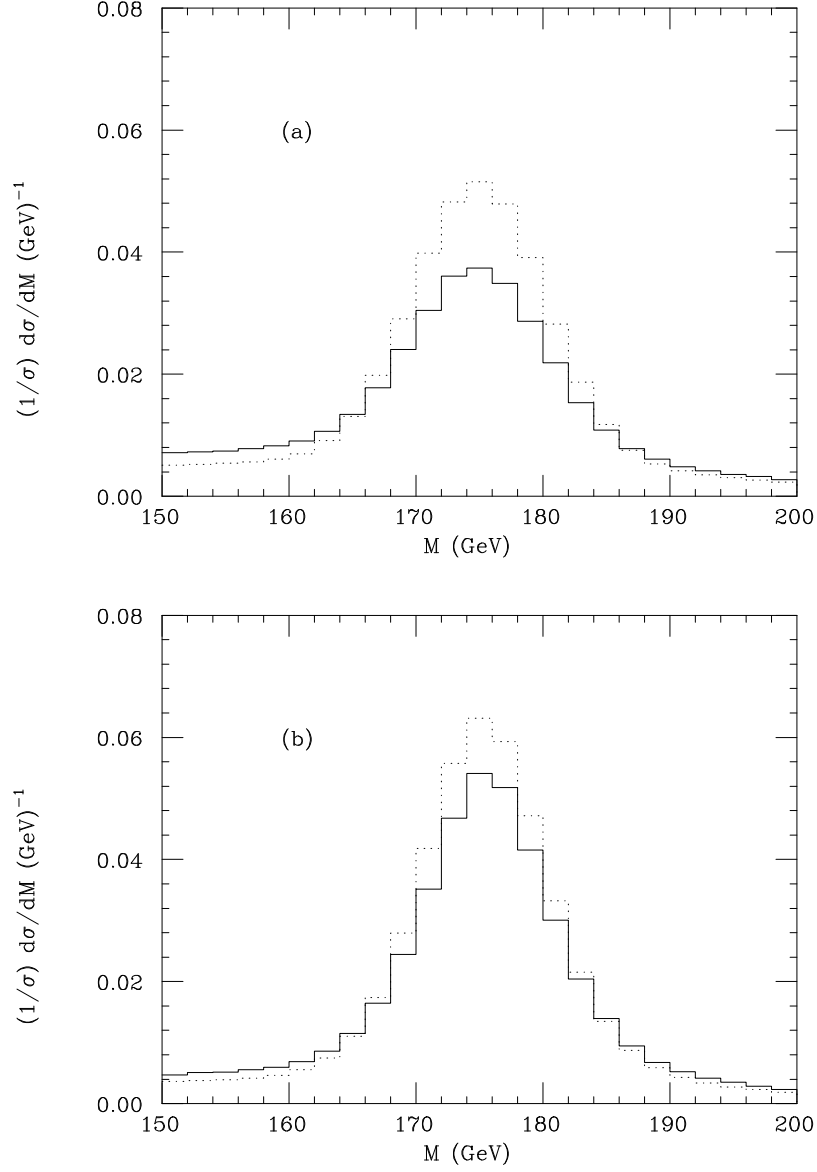


Fig. 10: Top mass reconstruction distributions with energy smearing of the final-state partons for $\sqrt{s} = 400$ GeV (a) in the all-jet mode and (b) in the lepton+jets mode. In both plots the dotted histogram is at tree-level and the solid histogram is at $\mathcal{O}(\alpha_s)$.